Atmospheric Correction and Its Application to an Analysis of Hyperion Data

Brian Cairns, *Member, IEEE*, Barbara E. Carlson, Ruoxian Ying, Andrew A. Lacis, and V. Oinas

***Abstract*—In this paper, tradeoffs between speed and accuracy for the atmospheric correction of hyperspectral imagery are examined. Among the issues addressed are the use of scattering calculations on a sparse spectral grid and consequent accuracy and speed tradeoffs, methods for minimizing the required number of quadrature points in multiple-scattering calculations, effects of the vertical profiles of aerosols and absorbing gases on atmospheric correction, and efficient approaches for including the effects of sensor variability (or imperfections) on atmospheric correction.**

***Index Terms*—Atmospheric correction, multiple scattering.**

I. Introduction

EVER SINCE digital imagery of the earth was first obtained there has been an interest in correcting the images for the effects of the atmosphere. One of the earliest radiative transfer approaches to simulating the atmosphere–surface system was presented by Turner and Spencer [1], and the effects of the atmosphere on image contrast were an early subject of study [2], [3]. During the 1980s, considerable work was done on the atmospheric correction of satellite imagery [4]–[6] and improvements in modeling and computational capabilities led to the development of the 5S atmospheric radiation model [7]–[9] which was used in [10] for the atmospheric correction of airborne visible/infrared imaging spectrometer (AVIRIS) data. Since 1990 numerous radiative transfer models [11]–[14] have been developed that can be used in atmospheric correction algorithms. Notable amongst these is MODTRAN that is a publicly available code that can provide high accuracy [15] and has been used in a number of different atmospheric correction approaches [16], [17]. Some of these radiative transfer codes use approximate methods [10], [12]–[14], while other approaches have emphasized the speed of calculations through the use of advanced numerical methods [18], or use the precalculation of lookup tables with exact methods [17]. The final choice of the radiative transfer code to use is determined by both the application and the availability of data with which to constrain the radiative transfer code [12].

The development over the last decade of high-quality remote sensing instrumentation that can simultaneously acquire imagery and the spectra of each pixel in the image has emphasized the need for fast and accurate atmospheric correction methods. As computers become faster there is less and less need to use "Empirical Line Methods" and most current efforts are oriented toward the use of accurate calculation techniques that have been optimized in some fashion [16]–[18]. The major sources of uncertainty in performing atmospheric correction are water vapor and aerosols. It is necessary, therefore, to include water vapor [19], [20] and aerosols [5], [21], [22] in the atmospheric correction calculations as accurately as possible. In the following, we describe a calculation approach to atmospheric correction that is fast, accurate, and simple such that it should be possible in future to perform atmospheric correction of hyperspectral data in the air, or at a ground terminal that is receiving the hyperspectral data from an aircraft. This method can use aerosols [21], [22] and water vapor [17], [20], [23]–[29] that are derived from the hyperspectral data, or information from other ground-based [30], or airborne sensors [31].

II. Methodology

A. Overview of the Problem

The radiance that is measured at the top of the atmosphere by a high spatial resolution (narrow field of view) instrument in a particular spectral channel j is given by the expression

$$I_j = \frac{\mu_0}{\pi \Delta\lambda_j} \int_{\Delta\lambda_j} r_j(\lambda) F_0(\lambda) R_A(\lambda)\, d\lambda \qquad (1)$$

in which r_j is the (properly normalized) spectral response in channel j; F_0 is the solar flux at the top of the atmosphere; and R_A is the reflectance of the atmosphere–surface system. The instrument spectral response, radiometric response and solar flux are important aspects of the final atmospheric correction and we briefly note the assumptions, or datasets that are used here. The requirements for instrument spectral response knowledge are discussed later in this paper and have previously been outlined in [32]. Instrument radiometric calibration is not discussed here except to note that radiometric accuracy is typically expected to be about 10% for hyperspectral instruments [33], [34], although a 2% accuracy is claimed for the improved AVIRIS instrument over the wavelength range 400–1800 nm [35]. The solar irradiance that is used here is based on a model that predicts the temporal variability of the spectral irradiance of the

Manuscript received July 14, 2002; revised February 6, 2003. This work was supported by the National Aeronautics and Space Administration New Millenium Program Earth Observing 1 Science Validation Team. Additional support for the acquisition of validation data was provided by Department of Energy's ARM program and by the Biological and Environmental Research Program (BER), U.S. Department of Energy, under Grant DE-FG02-02ER63351.

B. Cairns and R. Ying are with the Department of Applied Physics and Applied Mathematics at Columbia University, New York, NY 10027 USA (e-mail: bc25@columbia.edu).

B. E. Carlson and A. A. Lacis are with NASA Goddard Institute for Space Studies, New York, NY 10025 (e-mail: bcarlson@giss.nasa.gov; alacis@giss.nasa.gov).

V. Oinas is with SGT Inc., New York, NY 10025 (e-mail: voinas@giss.nasa.gov).

Digital Object Identifier 10.1109/TGRS.2003.813134

sun as a result of the influences of sunspot darkening and facular brightening [36]. This model replicates the observed temporal changes, explaining more than 80% of the variance [37]. The spectral irradiance distribution of this model is based on measurements by the SOLSPEC spectrometer [38] in the visible spectral domain (401 nm $< \lambda <$ 874 nm) and a theoretical spectrum at longer wavelengths [39]. The agreement among these spectra in their region of overlap is better than 2%, which is well within the absolute measurement uncertainty [38]. This temporally varying model was developed to facilitate more realistic simulations of solar-forced climate change on multidecadal and centennial time scales and allows for the historical reconstruction of the solar spectral irradiance at wavelengths from 0.1–100 μm, at 0.001-μm intervals, annually since 1600 and daily since 1882 [36]. Although temporal variations in spectral irradiance over the range typically observed by hyperspectral instruments is small, it is convenient to use a solar source function that provides a best estimate of solar spectral irradiance as a function of the solar cycle and it is this solar irradiance distribution that is used here. In the following discussion we are interested in the approximations that can be made to simplify the calculation of the atmospheric correction for an atmosphere with gaseous absorption.

We shall first discretize the response function of the instrument such that the change in response over any one of these discrete intervals is relatively small. In the case of typical hyperspectral instruments a reasonable discretization within the spectral responsivity of a given band is 1 nm. The expression given above can then be written as

$$I_j = \frac{\mu_0}{\pi N} \sum_{l=1}^{N} r_j^l F_0^l \frac{1}{\delta\lambda_l} \int_{\delta\lambda_l} R_A(\lambda)\, d\lambda \tag{2}$$

where

$$F_0^l = \frac{\int_{\delta\lambda_l} F_0(\lambda) r_j(\lambda)\, d\lambda}{\int_{\delta\lambda_l} r_j(\lambda)\, d\lambda} \tag{3}$$

and

$$r_j^l = \frac{\int_{\delta\lambda_l} r_j(\lambda)\, d\lambda}{\delta\lambda_l}. \tag{4}$$

The instrument response has been removed from the spectral integration over variations in atmospheric scattering and absorption, such that the calculation of atmospheric correction has been separated from the convolution over the specific instrument response function. This allows adjustments to the integration over instrument spectral response for "smile," temperature- (or shock) induced shifts, or other instrumental problems to be functionally and operationally separated from the effects on the observations that are caused by the atmosphere. The principal problem in atmospheric correction is, therefore, the calculation of the atmospheric properties integrated over some suitably chosen spectral integral $\Delta\lambda_l$. The properties that are required from these calculations are defined in the usual form of the equation that is used to model the effects of the atmosphere on the observed reflectance

$$R_{\rm obs} = R_A + T_2 \frac{R_S}{1 - sR_S} \tag{5}$$

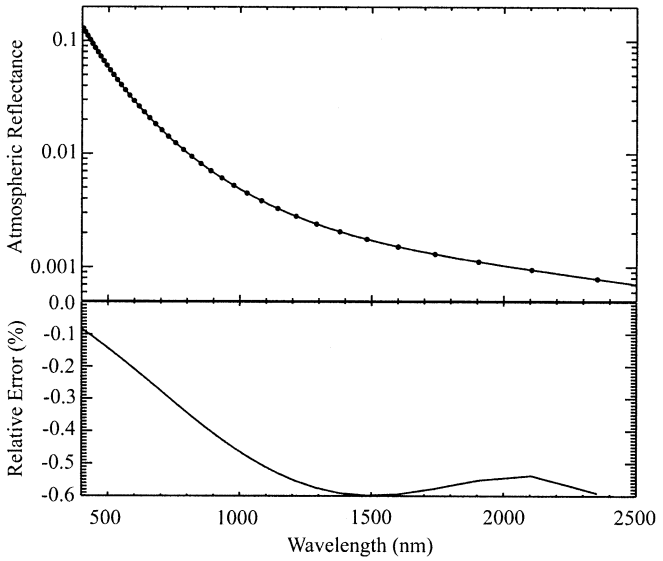

Fig. 1. (Top) Reflectance for an atmosphere containing molcules and aerosols (optical depth of 0.1 at 550 nm) calculated at 500-cm $^{-1}$ resolution from 400–2500 nm (line), together with the calculated reflectance at the midpoints, in frequency, of this discretization (filled circles). (Bottom) Relative error in interpolating the calculations with 500-cm $^{-1}$ spacing from 400–2500 nm to the midpoints of this spectral discretization.

where R_A is the atmospheric reflectance; T_2 is the two-way transmission including both diffuse and direct beam transmission; R_S is the surface reflectance; and s is the spherical albedo of the atmosphere when illuminated by the surface. It is important to note that when absorption is present and the atmosphere is vertically inhomogeneous the spherical albedo of the atmosphere is substantially different for illumination from below compared to when it is illuminated from above. We shall now concentrate on simplifications for calculating the atmospheric reflectance, the two-way transmission and spherical albedo of the atmosphere when illuminated by the surface over narrow spectral bands.

B. Scattering

If only scattering affected the observations from hyperspectral sensors then there would be little point in calculating the atmospheric properties at the resolution of the sensor, since aerosol and molecular scattering have smoothly varying spectral signatures that can be calculated at coarse resolution and then interpolated to the required spectral interval. In Fig. 1, we show that relative errors caused by the spectral interpolation of reflectance over the range 400–2500 nm are small (<1%) even with only 43 baseline spectral reflectance calculations. It is important that these points be distributed to capture the rapid variation of scattering properties at short wavelengths, while fewer points can be used at longer wavelengths where both the magnitude and the spectral variation of the scattering are weaker. The scattering calculations are, therefore, performed on a grid that is uniform in frequency with calculations performed every 500 cm^{-1} from 25 000 cm^{-1} (400 nm) to 4000 cm^{-1} (2500 nm), and interpolations are linear in frequency.

The other issue with regard to the speed and accuracy of multiple-scattering calculations, whether using doubling/adding

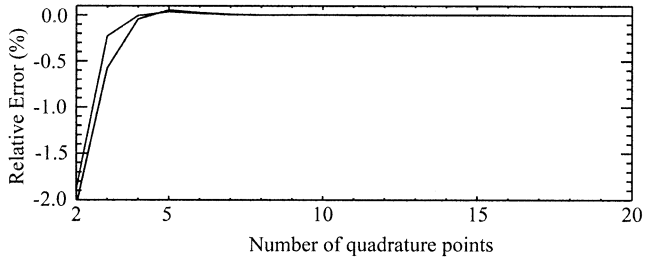

Fig. 2. Relative reflectance error as a function of the number of quadrature points when the reflectance is calculated at a pair of extra points (lower curve) and when the reflectance is calculated at a pair of extra points and single scattering is added back in exactly (upper curve).

or the discrete ordinates methods, is the number of quadrature points that are used. The doubling/adding method [40], [41] is used in the multiple-scattering calculations presented here although it should be noted that there is an intimate relationship between the doubling/adding and eigenmatrix methods [42], [43]. The doubling and adding method requires that the reflection and transmission functions be known for the layers to be added. The initial values of these functions are evaluated using two orders of scattering with an optical depth of $\tau \times 2^{-18}$ for the initial layer. The doubling method is then used within each homogeneous atmospheric layer to calculate the reflectance and transmission for a layer with an optical depth of τ [44]. Finally, the multiple-scattering calculations are completed by using the adding method to calculate the reflection and transmission properties of the vertically inhomogeneous atmosphere. The adding method also allows both the internal fields at each layer interface [45] and the emission probabilities [46] to be calculated. Thus, provided a layer interface is placed at the sensor altitude, it is straightforward to calculate radiances, for upward or downward looking sensors at any altitude, and the effect of perturbations (of the optical depth, or single-scattering properties) on those radiances [46], [47]. In Fig. 2, we show the results from using the doubling/adding method [44] with extra points at the required solar zenith and view zenith angles to perform multiple-scattering calculations with varying numbers of quadrature points. We also did similar calculations using the doubling/adding method but also separating out the single scattering and adding it back in exactly at the end of the calculation [45]. In both cases, it appears that if extra points are used for the specific view geometry of the sensor the required number of quadrature points can be reduced to only five or six. It should be noted, however, that in order to guarantee the accuracy of the calculation the required number of Gauss points should be evaluated for the first azimuthal term in the decomposition of the radiance field. Additional reductions in computational time can be obtained by automating [48] the stopping points for doubling calculations. Our approach uses a comparison of second-order scattering with the doubling calculation to terminate the use of the doubling process in the Fourier decomposition over azimuth and a comparison of first and second-order scattering to terminate the calculation of azimuthal terms. The separation of single scattering together with approximate calculations for higher orders of scattering has been previously used to provide a relatively accurate and very fast calculation of the radiation field [49]. In the method presented here, the removal of single scattering from the results and then adding it back in exactly ensures that the calculation has a guaranteed level of accuracy, but is still efficient. Although approximations are used in the calculation of higher order scattering, they are only used when they have a specified level of accuracy compared to a more accurate calculation. In this case, the tolerance is for reflectance differences of 10^{-6}, although this can be adjusted to suit the particular application.

The conclusions that can be drawn from the results presented above are as follows. If it is possible to decouple absorption and scattering more accurately than simply separating the two processes then scattering calculations would only be required on a coarse spectral grid. If "extra" quadrature points are used, multiple-scattering properties can be calculated very rapidly and accurately for any given dataset, using the best possible estimates for optical depth and scattering phase function available, rather than using precalculated tables of scattering properties, or generic aerosol models.

C. k Distributions

The only atmospheric property that varies rapidly on a 1-nm spectral scale is absorption by gases. The most accurate calculations of atmospheric reflectance use calculations at a sufficiently high spectral resolution that the absorption lines of the gases are resolved. These are called line-by-line calculations. For our line-by-line calculations, we use the HITRAN 2000 database that includes the recent updates to the near-infrared (NIR) band strengths [50]. We extract the line strengths, air-broadened half widths, self-broadened halfwidths, energy levels, and line positions from the database. To model the effect of pressure and Doppler broadening on line shape, we use the Voigt profile throughout the atmosphere; line wings are truncated 25 cm^{-1} from the line center and the spectral resolution used is 0.005 cm^{-1}. We use several optimizations to reduce computing time but maintain computational accuracy. For example, absorption lines that are too weak to contribute significant absorption ($<0.01\%$) over the range of absorber amounts of interest are eliminated, and we combine closely spaced overlapping lines. The full pressure and temperature dependence of absorption line shapes as well as line wing contributions from outside the immediate spectral interval are explicitly included in the calculations. The line-by-line calculations are used to provide the absorption coefficients in each spectral band and in each atmospheric layer at a fine spectral resolution. This information serves as the basis of the subsequent k distribution calculations.

The k distribution is based on a reorganization of the spectral integral such that it becomes an integral over the fraction of lines with a given strength. The k distribution and its properties have been discussed at length elsewhere [51], [52]. In Fig. 3, it is shown how the k distribution works. On the left is shown the variation of the O_2 column absorption with wavelength in the 760-nm spectral interval. The figure on the right shows the cumulative histogram of absorption coefficients in this same spectral interval. It is more accurate, given a limited number of discretization intervals, to discretize the distribution on the right, provided there is no subband variation of other atmospheric properties such as scattering. For polydisperse scatterers the spectral variation of scattering properties is smooth on

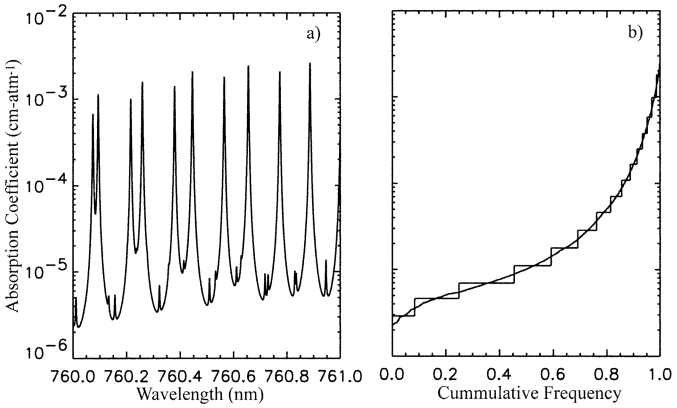

Fig. 3. (a) Variation of the O_2 absorption coefficient as a function of wavelength between 760–761 nm in the A-band and (b) plotted as a cumulative histogram with a set of k values based on 15 discretization intervals.

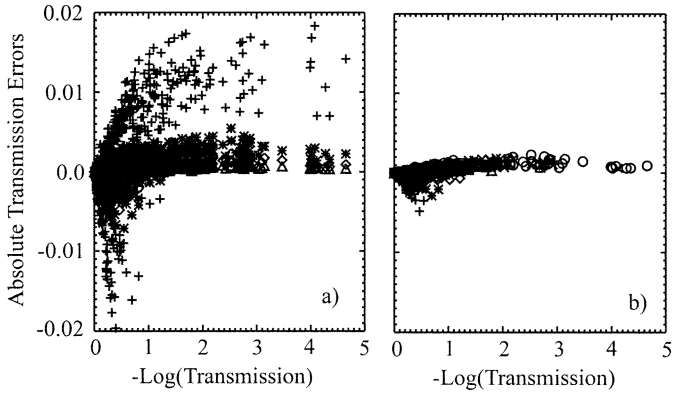

Fig. 4. This figure shows the absolute error of k distribution calculations of transmission with 1-nm resolution compared with line-by-line calculations for water vapor over the spectral range from 900–1000 nm. The comparison is over a range of water vapor total column amounts from 0.25–16.0 precipitable centimeters. The k distributions were tuned to provide exact results for a column amount of water of 2.0 precipitable centimeters with an airmass of 2.5 (i.e., 5 precipitable centimeters is the effective column amount). This airmass was chosen as being indicative of a nadir viewing sensor with solar zenith of 48°. (a) Transmission accuracy for k distributions with 5, 10, 15 and 20 intervals shown as crosses, stars, diamonds and triangles, respectively. (b) Transmission accuracy as a function of water vapor amount for k distributions with 15 intervals, where the water vapor amounts are 0.25, 0.5, 1.0, 2.0, 4.0, 8.0, and 16.0 precipitable centimeters shown as crosses, stars, diamonds, triangles, squares, diagonal crosses, and circles, respectively.

a 1-nm scale and can be considered to be essentially constant within such a bandwidth. Thus, the spectral integration shown in (1) can be transformed into an integration over absorption strength.

D. Accuracy of k Distributions

As noted in [52] the k distribution can be tuned to provide exact transmission values for a particular absorber amount. The absorber amount for which the k distributions are exact in this application uses an airmass of 2.5 (e.g., nadir viewing and solar zenith angle of 48°) and column absorber amounts of two precipitable centimeters of water vapor with typical column amounts for the well-mixed gases and CO. If it is required that the k distribution be accurate over a wide range of absorber amounts, then a reasonable number of absorption, or g, intervals must be used. The number of required absorption intervals is determined by the required accuracy and range of absorber amounts over which this accuracy is to be maintained. In Fig. 4, it is shown that the absolute errors in direct beam transmission can be kept below 0.005 over a wide range of absorber amounts using 15 absorption intervals.

E. Vertical Distribution of Absorption

We have not, thus far, discussed the vertical variation of absorption. The monotonic ordering of absorption coefficient strengths in the k distributions in each vertical layer implicitly preserves the monochromatic structure of the atmosphere at different pressure levels, thus simulating the monochromatic structure of the atmosphere at a fraction of the line-by-line computing cost. For the purposes of atmospheric correction, this method would require the calculation of the reflectance and transmittance in each layer for each absorption interval. This can be represented by the equation

$$R_A = \sum_i \left(\sum_z R_A^z(k_i u) \right) \Delta g_i \tag{6}$$

in which the summation over vertical layers (z) is a formalism indicating an adding calculation [44] and R_A is the atmospheric reflectance. Here we have suppressed the dependencies of reflectance on other atmospheric properties, and it should be noted that the same summations are required for all the other quantities used in atmospheric correction. Although the use of the k distributions in each vertical layer provides very high accuracy compared with line-by-line calculations, it is not always necessary to have such accuracy for atmospheric correction. In particular, atmospheric correction only requires that the upwelling radiance be simulated accurately at the top of the atmosphere, or at the flight level of an aircraft. The radiance at the centers of absorption lines, or in this case the k values with the strongest absorption, will contribute a negligible amount to the band integral, since most of this radiation is absorbed. The majority of the observed upwelling radiance will, therefore, come from the wings of absorption lines. The wings of spectral lines in the troposphere, where the majority of the gaseous absorption occurs, are Lorentzian and the absorption strength in the wings is, therefore, proportional to the line strength and the line width (and consequently pressure). Although the line width, the vibrational partition function, the rotational partition function and the lower state population probability all depend on temperature we may expect that the dominant dependency of the strength of the correlated k values as a function of altitude will be a linear dependence on pressure because of the significantly greater variation in atmospheric pressure than absolute temperature.

This behavior is demonstrated empirically in Fig. 5 where the variation of the normalized k values with pressure for particular g intervals is shown for all the k distributions in the spectral range from 920–930 nm. The k intervals are ordered from smallest to largest, and the lower k intervals should, therefore, correspond to either line wings, or the centers of very weak lines, while the higher k intervals will correspond to line centers. As discussed above, those k intervals that come from line wings should have a linear dependence on pressure of their k values as can be seen for the third and seventh k interval. Those

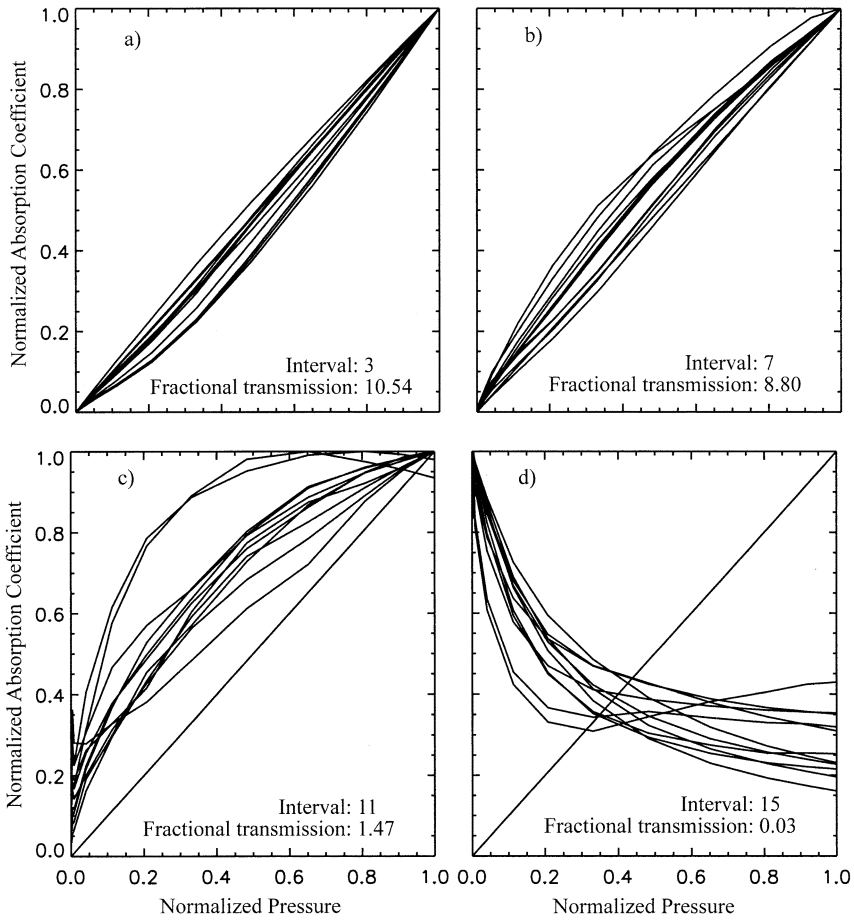

Fig. 5. These figures show the variation of k value with pressure for the (a) third, (b) seventh, (c) 11th, and (d) 15th k absorption interval for all the 1-nm spectral bands between 920–930 nm.

k intervals that are dominated by contributions from line centers will not have such a simple dependence on pressure as can be seen for the 11th and 15th k intervals. However, since for the purposes of atmospheric correction we are not interested in the vertical distribution of heating, those k intervals that contribute the majority of the transmitted and reflected light are the ones which are of relevance. As can be seen from the annotations on Fig. 5 the fraction of transmitted light contributed by the 11th and 15th k intervals is small compared with that contributed by the third and seventh k intervals. This feature of absorption and the consequent insensitivity of atmospheric reflection and diffuse transmission to the detailed distribution of absorption with altitude near line centers suggests an alternative approach to calculating the reflectance in an absorbing band. In this approach, we calculate the reflectance for multiple absorption values, that cover the range that may be expected, with a vertical distribution of the absorption that is appropriate for a particular gas, such as water vapor *viz.*,

$$R_A^T(\tau_{\rm abs}) = \sum_z R_A^z \left[\tau_{\rm abs} u_z p_z \Big/ \left(\sum_z u_z p_z \right) \right] \quad (7)$$

with u_z being the profile of absorber amount and p_z the pressure for the vertical discretization used in the multiple-scattering calculations. We found that using 21 absorption optical depths log-linearly spaced from zero to 10^5 provided sufficient range and accuracy. The reflectance for a particular spectral band can then be calculated by interpolating the precalculated multiple absorption optical depths to the column absorption values required by the k distribution for that band and summing with appropriate weights, i.e.,

$$R_A = \sum_i R_A^T(k_i u_{\rm tot}) \Delta g_i. \quad (8)$$

This approach separates the actual details of gaseous absorption from the scattering calculation, which allows the scattering calculations to be performed on the type of coarse spectral grid described in Section II-A above and then interpolated to the spectral interval of interest. We have, therefore, transformed the problem of multiple radiative transfer calculations (e.g., 2100 spectral intervals for calculations at 1nm spacing from 400–2500 nm and 15 absorption values for accurate use of k distributions) to fewer radiative transfer calculations (43 with 21 absorption values) and some simple interpolations. It should be emphasized that the k distributions used in the final summation over absorption optical depth are based on exact line-by-line calculations (no assumptions about temperature, or pressure dependence are made) for a 12-layer standard atmospheric profile and that the direct beam transmission is always calculated using these k distributions, which ensures the accuracy of the direct beam calculation. Other atmospheric profiles (e.g., tropical, midlatitude winter, etc., or measured)

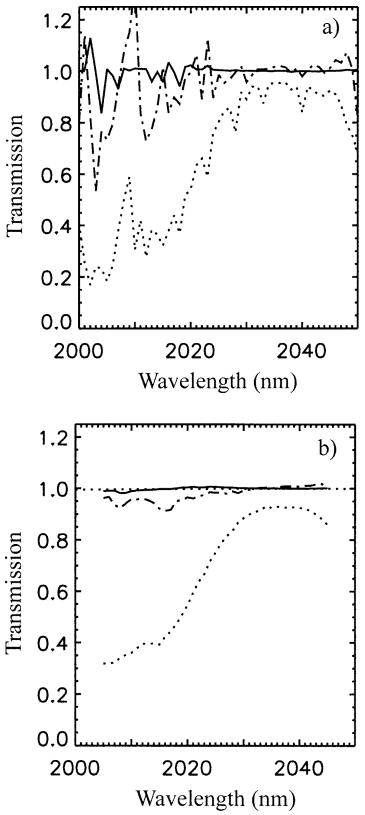

Fig. 6. Line-by-line transmission calculations for (a) 1-nm and (b) 10-nm spectral integrations are shown as a dotted line. The ratio of the random overlap approximation calculation of transmission to the line-by-line calculation of transmission is shown by a solid line at (a) 1-nm and (b) 10-nm spectral resolution. The ratio of the maximum overlap approximation calculation of transmission to the line-by-line calculation of transmission is shown by a dot-dashed line at (a) 1-nm and (b) 10-nm spectral resolution. A dotted line at a transmission level of 1.0 is shown for reference.

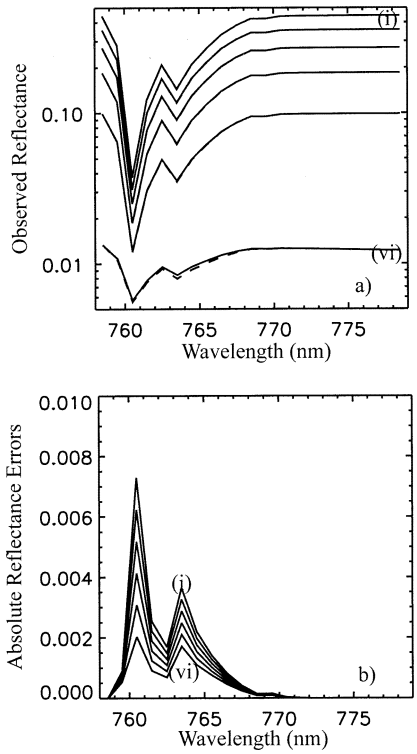

Fig. 7. (a) Observed reflectance calculated in the O_2 A band using exact calculations every 1 nm (solid lines) and using our approximate, spectrally interpolated with pressure weighted distribution of absorption, approach (dashed lines). The surface reflectance is Lambertian and has a value of 0.0, 0.1, 0.2, 0.3, 0.4, and 0.5 (shown as lines with increasing magnitude). (b) The absolute surface reflectance error obtained when the observed reflectances simulated using the exact calculations are atmospherically corrected using the approximate approach (lines with increasing magnitude correspond to surface Lambertian reflectances of 0.0, 0.1, 0.2, 0.3, 0.4, and 0.5).

can be added as required by simply recalculating the k distributions from the HITRAN 2000 database.

F. Overlap of Gaseous Absorption Bands

Where the absorption bands of different gases overlap a simple application of the correlated k distribution is not possible unless there is a fixed ratio of absorber amounts of the two gases. When the absorber amounts vary, for example where water vapor overlap with carbon dioxide and nitrous oxide near 2000 nm, then one of two approaches can be used. The simpler approach is to take the direct product of optical depths from the k distributions. This approach in which gaseous absorption strengths of similar ordering are multiplied with one another is analogous to a maximally overlapped model of the absorption of the two gases. Although this approach is simple it does require that the k distributions for the two, or more, gases use the same g intervals over the spectral interval of the overlap. The more complicated approach is to take the outer product of optical depths from the k distributions that are then rebinned back to the original number of k intervals. This approach in which all the k intervals from one gas are multiplied with all k intervals from the other gas and then rebinned is analogous to a randomly overlapped model of the absorption of the two gases. This is the approach suggested by [52] and although somewhat more complicated to implement it does have the advantage that the g intervals for each gas can be chosen for each gas separately. Furthermore, as shown in Fig. 6 the random overlap approximation is more accurate near 2000 nm where there is overlap between water vapor, carbon dioxide and nitrous oxide absorption. In particular at the 10-nm spectral resolution typical of hyperspectral sensors the random overlap approximation gives typical errors of the order of 1% in the region of strong carbon dioxide and water vapor absorption, while the maximum overlap approximation can give errors of 10%. It should be noted that in general neither the maximally, nor the randomly overlapped methods of combining correlated k-distributions guarantee good results and the two different approaches should be compared against exact line-by-line calculations in order to determine which approach is to be preferred and what magnitude of errors may be expected if correlated k-distributions are used.

G. Overall Accuracy

As we showed above, the spectral interpolation of a coarse spectral mesh of scattering calculations is extremely accurate for purely scattering atmospheres. Therefore, it remains to show how the combination of scattering and vertical distribution of absorption approximations affects the overall accuracy of the atmospheric corrections that can be achieved using these methods. In Figs. 7 and 8, examples of the accuracy of these approximations are given for spectral bands where we might reason-

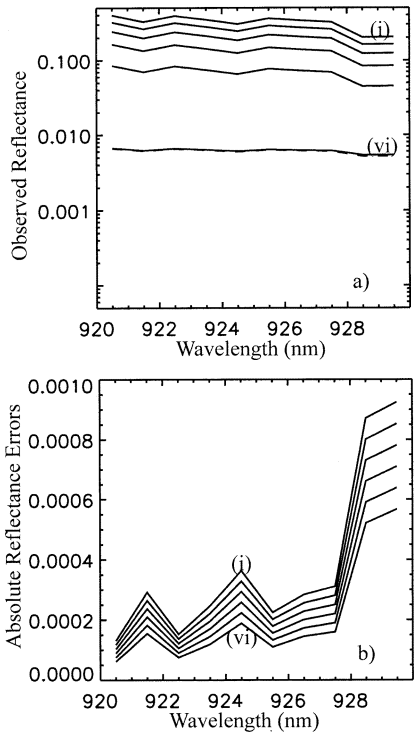

Fig. 8. (a) Observed reflectance calculated in an H_2O band using exact calculations every 1 nm (solid lines) and using our approximate, spectrally interpolated with pressure weighted distribution of absorption, approach (dashed lines). The surface reflectance is Lambertian and has a value of 0.0, 0.1, 0.2, 0.3, 0.4, and 0.5 (shown as lines with increasing magnitude). (b) The absolute surface reflectance error obtained when the observed reflectances simulated using the exact calculations are atmospherically corrected using the approximate approach 5 (lines with increasing magnitude correspond to surface Lambertian reflectances of 0.0, 0.1, 0.2, 0.3, 0.4, and 0.5).

ably expect to have significant scattering and absorption *viz*., the oxygen A-band and the wings of the water vapor band at 945 nm. The "exact" calculations use the actual correlated k-distributions with the correct distribution of gaseous opacity and absorber amounts for a United States standard atmosphere.

The approximate calculations use the method described above which we will summarize here. In this method, multiple-scattering calculations are performed on a coarse spectral grid for a range of absorption optical depths that covers the values expected for the spectral range of 400–2500 nm. The vertical distribution of opacity (absorption coefficient) in these calculations is proportional to pressure and the absorber amount is the correct amount for the dominant gas present (e.g., well-mixed gases, or water vapor). To calculate the combined effects of absorption and scattering for a particular spectral band the first step is to interpolate (linearly in frequency) the scattering calculations, for a range of absorption optical depths, to the desired spectral location. The next step is to interpolate the scattering calculations to a set of absorption optical depths that are determined by the k-distributions for the entire column for that band. The final step is to integrate (sum) the reflectance, diffuse transmittance and spherical albedo of the atmosphere over their fractional contribution at each absorption optical depth using the weights (associated with these different absorption optical depths) taken from the k-distributions.

The only significant assumption in this process is using a linear dependence on pressure for the absorption coefficient and it is this assumption that is being evaluated in Figs. 7 and 8. These figures show that the error in atmospheric correction caused by calculating atmospheric multiple-scattering effects using pressure weighted absorber amounts at coarse spectral resolution that are then spectrally interpolated is quite small. This means that the reflectance can be precalculated, or calculated for the particular conditions present, with an appropriate vertical distribution of absorption that is representative of all the k intervals that make a significant contribution to the observed radiance. Over the spectral region of interest here (400–2500 nm), it is necessary to have at least two different vertical distributions of absorption, one for well-mixed gases (CO, CO_2, CH_4, N_2O, O_2) and one for water vapor, since the scale heights of these gases are very different, and also to choose between these vertical distributions in spectral domains where there is line mixing. CO is treated as a well-mixed gas because of the absence of readily available information that would allow for a better treatment. Since multiple-scattering calculations are only required on a sparse grid, these calculations can be done beforehand and used as lookup tables, or calculated at the time with detailed aerosol size distributions and refractive indices.

H. Other Issues

As well as line absorption it is also necessary to include absorption from continuum features in the calculation of the atmospheric correction functions. Since absorption by ozone is predominantly above most atmospheric scattering the absorption by this gas and nitrogen dioxide are treated as being physically separated from (i.e., above, in the stratosphere) all the scattering, and therefore, they only affect the direct beam transmission. Other continuum absorption features that are included in our scattering calculations, with appropriately pressure weighted vertical distributions, are the water vapor continuum [53] (self and foreign broadened) and the O_2–O_2 continuum. The final results of the atmospheric correction calculations are the atmospheric reflectance, the spherical albedo of the atmosphere illuminated from below, two-pass direct beam transmission and two-pass diffuse transmission at one nanometer resolution that can be convolved over the instrumental response. These are shown in Fig. 9 for a typical atmosphere (1 precipitable centimeter water vapor and optical depth of 0.1 at 550 nm). An outstanding issue that remains to be resolved is the best method for dealing with adjacency effects, since it is not clear that the current approximations [54]–[56] are adequate when adjacency effects become a serious problem. Furthermore, measurements of the aerosol vertical profile with which to constrain the scale length over which adjacency effects will operate are not typically available.

III. Application of Atmospheric Correction Calculations to the Analysis of Hyperion Data

A. Focal Plane Array Characterization

The atmospheric correction approach described above emphasized the ability to trade accuracy and speed by reducing the spectral sampling of scattering calculations and controlling the accuracy and speed of the k distribution integrations by varying the number of absorption intervals that are used. The emphasis

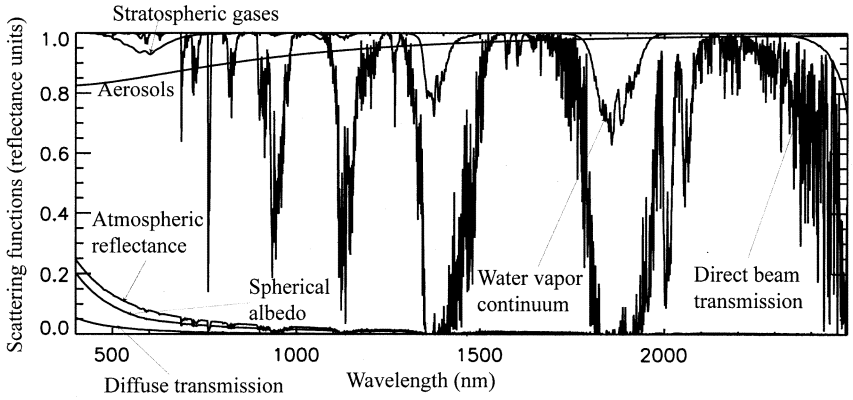

Fig. 9. Atmospheric scattering and absorption properties (labeled in the figure) calculated at one nanometer resolution using 15 k intervals in each spectral band where line absorption is present. The vertical distribution of absorption within the multiply scattering atmosphere is as described in Section II-E and the combined scattering and absorption properties of the atmosphere are being calculated with this approximate distribution of gaseous opacity.

on speed is particularly relevant to the analysis of data from two-dimensional (2-D) focal plane arrays (2-D FPAs) which are becoming more common in commercial hyperspectral imagers and which is the approach used by the Hyperion instrument. This is because the assumption that all pixels of a cube have the same spectral calibration, as is the case with single IFOV instruments, is not necessarily valid for instruments that use an area array detector. Thus, the spectral registration of the atmospheric correction function may have to be allowed to vary across the instrument swath placing a greater computational burden on the atmospheric correction of a hypercube.

There are two principal sources of spectral deviations that can cause the spectral response of a 2-D FPA spectrometer to vary with spatial location: Smile and rotational misalignment. Spectral smile is caused by curvature of the image of the slit formed on the FPA. Curvature causes the response center of a given sample to vary across the spatial direction of the FPA. Rotational misalignment is caused when the slit is not parallel with the diffraction grating. In a manner similar to that of smile, this misalignment causes response center variations across the spatial direction of the FPA. Spectral offsets that affect all pixels in the same way are also a source of errors in atmospheric correction but can be identified using the same methods as for smile and rotational misalignment. Although smile and rotational misalignment exist in some 2-D FPA imaging spectrometers careful design can eliminate, or mitigate these problems. Given the processing problems that such instrumental flaws cause it is important that appropriate design trades be made to minimize these flaws and an example of this type of analysis has been presented in [57] for two different types of spectrometer.

For the resolution of typical land surface spectral features, spectral calibrations need not be orders of magnitude better than the spacing between bands. However, in instances where subtle differences must be resolved or atmospheric effects must be removed, accuracies must approach 1/100th the width of the bands, which in the case of Hyperion would require spectral calibration accuracies of 0.1 nm [32], [58]. However, rather than regarding the spectral requirements for accurate atmospheric correction as a burden, one can regard them as a useful tool for providing a "bootstrap" spectral calibration by using major atmospheric absorption features to determine the spectral registration of the hyperspectral instrument. Although the spectral registration is then only determined for the bands in the vicinity of the absorption feature that is being used, one can then apply the shift that is estimated from the "bootstrap" method to the band center locations of all the spectral bands that are provided by the laboratory spectral calibration of the instrument. This approach of using the atmosphere, or sun, as a source for spectral calibration has been used by many scientists, including those working with the Airborne Visible/Infrared Imaging Spectrometer (AVIRIS) [59]–[61] and is used to operationally calibrate satellite spectrometers [62]. This approach assumes that 1) the instrument is well designed and fabricated such that the spectral deviations of smile, rotational misalignment and spectral offsets described above are the principal source of calibration uncertainty and 2) that the "bootstrap" estimates of band locations do not deviate from the laboratory determined band locations by more than the band widths. This second requirement is based on two considerations. First, if a spectrometer shifts by many bandwidths from the laboratory determined locations then we must be concerned that the instrument is unstable even during the acquisition of a single hypercube. Second, although it is certainly possible to locate and identify a spectral band (or spectrum) that is shifted by many bandwidths from its nominal registration this represents an onerous processing task that would require a sequential approach using the cospectrum (Fourier transform of the correlation between the actual and reference spectra) to provide a crude identification of band location and a search to refine that determination. The use of such a general, sequential, approach is not presented here, since we expect all well-designed instruments to meet criterion 2) above. Since existing hyperspectral instruments use separate spectrometers for the visible NIR (VNIR) and shortwave infrared (SWIR) spectral domains the absorption features that are available to perform the "bootstrap" calibration of the two spectrometers are different, and therefore, we shall discuss the two spectral domains separately.

1) VNIR Spectrometer: In the VNIR, the best absorption band to use for evaluating the spectral calibration of a spectrometer is the oxygen A-band, which is strong, narrow, and has a well-defined depth, since oxygen is a well-mixed gas. The radiances in the vicinity of the oxygen A-band are first normalized by a proxy surface reflectance that is derived by linearly interpolating between the bands that are in atmospheric windows on either side of the A-band. This type of normaliza-

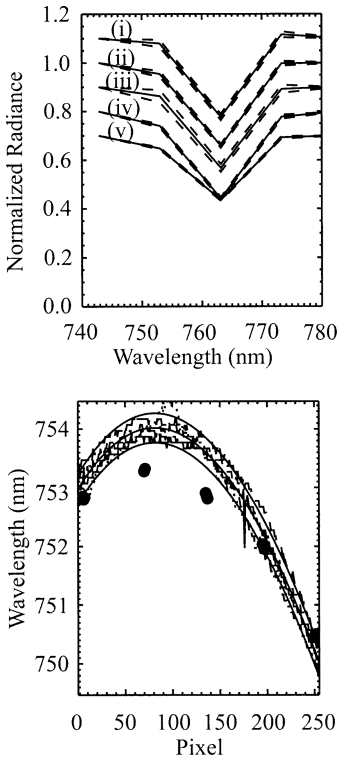

Fig. 10. (a) Mean normalized radiance (solid lines) and ± 1 standard deviation from the mean (dashed lines) in the vicinity of the oxygen A-band for Hyperion data taken over GVWD, Coleambally (two datasets) SGP and Arizaro are labeled as (i), (ii), (iii), (iv), and (v), respectively. (b) The spectral locations for Hyperion band 40 shown as a function of pixel determined from an analysis of normalized radiances for GVWD (dotted), Coleambally (dashed and dotted-dashed), SGP (dot-dot-dot-dashes), and Arizaro (long dashes). The smooth polynomial fit to all the estimates is shown as a thick solid line, and the range of ± 0.25 nm from this estimate is shown as solid thin lines. The filled circles are based on our analysis of prelaunch spectral response measurements of the Hyperion sensor performed at TRW.

tion is used in the calculation of the continuum-interpolated band ratio [63] and the linear regression ratio [17] and is intended to reduce the effects of surface spectral variability on the subsequent analysis. The average and standard deviation of these normalized radiances along a line of an image is then calculated for each location across a row. The standard deviation is used to test the assumed spectral linearity of the surface spectral reflectance and the uniformity of this assumption over a range of surface types. If this assumption is wrong, the standard deviation is large and indicates that an alternative approach is required, since the inappropriate use of a spectral slope in the surface reflectance can bias the estimate of the location of the oxygen A-band. The means and standard deviations for five sets of Hyperion data from GVWD, Coleambally (2), the Atmospheric Radiation Measurement (ARM) Southern Great Plains (SGP) site, and the salt flats of Arizaro are shown in Fig. 10(a), where it is clear that the standard deviations of the normalized radiances are relatively small. The following analysis is applied to the mean along a line of the oxygen A-band normalized radiances (and ± 1 standard deviation about the mean), since the main instrumental defects that we are trying to identify are the spectral registration of the instrument and the variation of this spectral registration as a function of location in the image (i.e., location across a row).

The application of the "bootstrap" method to the determination of spectral locations from normalized oxygen A-band radiance data is then straightforward. A complete set of atmospheric correction functions are calculated by shifting the band centers of the instrument response functions with respect to the nominal values provided by TRW in steps of 0.1 nm from -3.5 to 3.5 nm. The normalized radiance data in the region of the oxygen A-band is then atmospherically corrected with a sequence of different spectral registrations. This atmospherically corrected data is then fitted with a smooth (second-order) polynomial. If the underlying surface spectral reflectance is a smooth function of wavelength then the rms difference between the corrected reflectance spectrum and the smooth polynomial will be minimized when the correct spectral registration is being used, since the oxygen A-band is not a smooth function of wavelength. The identification of the correct spectral registration is, therefore, performed by finding the atmospherically corrected spectrum that is smoothest. It should be noted that a linear variation across the band is already corrected for in the normalization process described above and that the polynomial fit is only used to determine if the spectrum is smooth or not: not to determine the band location. This "bootstrap" process is performed separately for each location across a row, and the determinations of the spectral shift of the band centers with respect to their nominal values for the VNIR FPA are shown in Fig. 10(b) for the five different datasets. In this figure, only the analysis of the mean normalized radiance for a particular dataset is shown, since there is more variability between sites than for the analysis of a particular site. The uncertainty in the analysis for a particular site, obtained by propagating the standard deviations of the normalized radiances through the bootstrap estimate is ± 0.1 nm, while the variation across all sites is ± 0.25 nm as shown in Fig. 10(b). The variation of the spectral response determined from prelaunch characterization is also shown to indicate the similarity of the magnitude of the smile between pre and postlaunch analyses.

2) SWIR Spectrometer: The bands used for the "bootstrap" spectral calibration of the SWIR spectrometer are the carbon dioxide band at 2000 nm and the water vapor band at 1125 nm. Both bands were used in this analysis because each has some problems in its use for evaluating the spectral response of an FPA. The water vapor band has reasonable strength even for water vapor amounts as low as 0.5 precipitable centimeter, but it is a less desirable band than the oxygen A-band for this application because water vapor is not a well-mixed gas and the band is also quite wide. Therefore, one must know (or estimate) the water vapor amount if this band is to be used in the "bootstrap" spectral calibration, and since the band is so broad, the estimate of the spectral registration is less accurate (it has a broader minimum). It is certainly possible to perform a 2-D search for both the water vapor amount and the spectral registration that minimizes the spectral variability of the atmospherically corrected reflectance in this water vapor band, but this further degrades the accuracy with which the spectral registration can be determined. The carbon dioxide band at 2000 nm is strong; its two branches are fairly narrow; and carbon dioxide is a well-mixed gas. Unfortunately, at this time the atmospheric correction model has cleaner windows between the two branches of

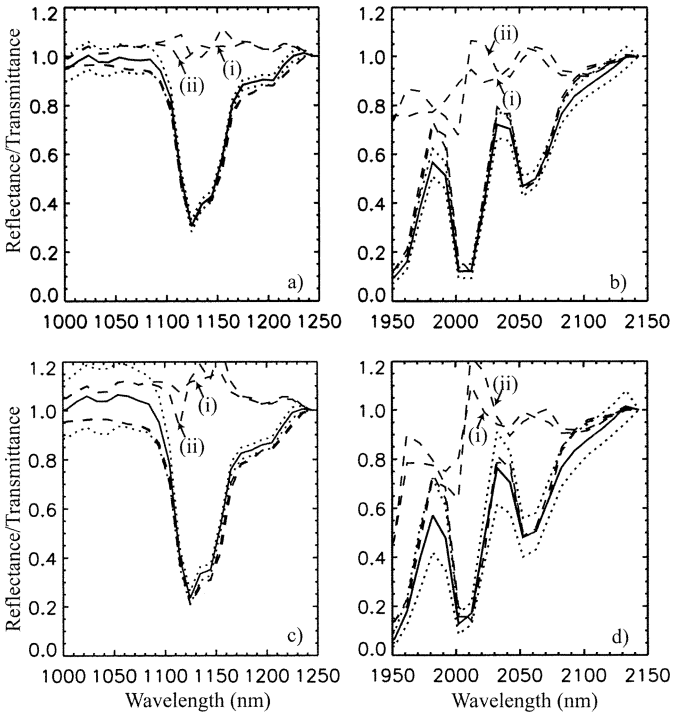

Fig. 11. In each figure the mean (solid line) and ± 1 standard deviation (dotted lines) for the spectral reflectance normalized by the spectral reflectance in the nearest atmospheric window of a single scan line are shown. The lower pair of dashed lines are the calculated transmission normalized by the transmission for the same spectral window as used to normalize the spectral reflectance. The upper pair of dashed lines are the normalized spectral reflectance divided by the normalized transmission. The dashed lines labeled (ii) use the nominal band center locations provided with the data, while the dashed lines labeled (i) have a $+1.5$-nm shift with respect to the nominal values. Figures (a) and (b) are examples of data from the SGP and (c) and (d) are examples of data from Coleambally in NSW.

the carbon dioxide band and between the carbon dioxide band and the water vapor band at 1900 nm than the Hyperion data, and it is, therefore, not possible to simply minimize the residuals of the atmospherically corrected spectral reflectance. As shown in Section II-F, line-by-line calculations do not show any significant problems with the random overlap approximation that is being used in the atmospheric correction model, and the problems with atmospherically correcting the Hyperion data in this spectral region can currently only be ascribed to real spectral variability in the surface, detector nonlinearity, or out-of-band issues. It should be noted that neither of the detector issues are regarded as particularly plausible, but are noted here for completeness. At present we are, therefore, using the spectral shape of the window and absorption band centers of the carbon dioxide band at 2000 nm to evaluate the spectral registration determined from an analysis using the water vapor band at 1125 nm. By combining an analysis of the water vapor band using data for which the water vapor amount is known with an analysis of the carbon dioxide band, one can determine the spectral registration of the SWIR spectrometer. In the case of Hyperion SWIR spectrometer, there is no discernable smile, or other pixel-dependent spectral regisration issues. However, there does appear to be a small shift in the SWIR spectral registration of the on-orbit data with respect to the laboratory-determined spectral registration provided with the data. This is shown in Fig. 11. The dashed lines labeled with a (i) in this figure use transmission values calculated using band centers that are shifted $+1.5$ nm with respect to the nominal band centers [shown as dashed lines labeled with a (ii)] and appear to match the spectral shape of the data somewhat better. However, the poor agreement between the calculated transmission values and the Hyperion data in the spectral windows of the 2000-nm carbon dioxide band mean that this analysis is far less robust than that for the VNIR spectrometer that uses the oxygen A-band.

B. Determination of Water Vapor Amount

Papers that relate total column water vapor to the transmission of radiation in the NIR water vapor bands date back to the early part of the last century [64], [65]. A review of this literature and the history of these ground-based upward-looking measurements was recently presented in [66]. In 1945, Foster and Foskett [67] used their spectrometer as a sun photometer with slits at 940 and 1010 nm to measure within and outside the water band. It was not until more recently that similar differential absorption methods were applied to downward-looking imaging spectrometer [10], [16]–[20], [23]–[27] and channel radiometer measurements [28], [29] in order to estimate column water vapor amounts. The determination of water vapor amount presented here is almost identical to the "bootstrap" analysis of the oxygen A-band described above, which is itself similar to the approach for estimating water vapor amount previously used in [20]. In the implementation used here the spectral reflectance data over the spectral range 1050–1240 nm is first normalized by the spectral reflectance in the spectral window at 1240 nm for that pixel. This spectral band is used because the water vapor amounts in the images of interest are relatively small and because there are issues with the spectral overlap and cross calibration of the SWIR and VNIR detectors of the Hyperion sensor in the 945-nm water vapor band. The normalized spectral reflectance is then divided by the calculated (for a particular water vapor amount) spectral transmission over the spectral range 1050–1240 nm (normalized by the calculated spectral transmission at 1240 nm): we will call this function the transmission normalized spectral reflectance. A polynomial of second, or third, order is then fitted to the transmission normalized spectral reflectance and the difference between the polynomial, and the transmission normalized spectral reflectance is calculated. The rms of this difference will have a minimum when the transmission normalized spectral reflectance is smoothest. Provided the land surface spectrum is smooth, the transmission normalized spectral reflectance will be smoothest when the spectral transmission is calculated using the correct water vapor amount. The estimate of water vapor amount can, therefore, be reduced to the search for the minimum of the rms difference between the transmission normalized spectral reflectance and its best fit polynomial as the water vapor amount is varied.

The most obvious confounding factor in such a search is the surface spectral reflectance having greater variability than the polynomial can model, or projecting real surface spectral variability into the water vapor retrieval. This may be a problem when the land surface is vegetated [20], because of

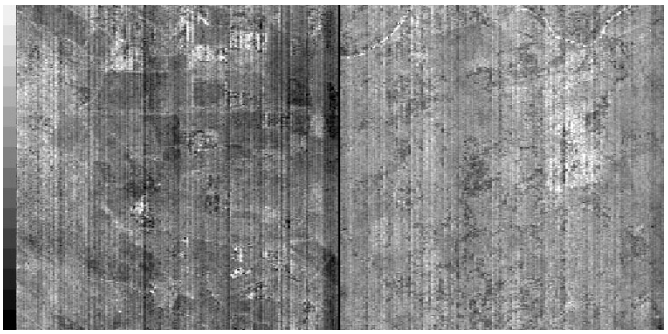

Fig. 12. The two panels show water vapor images of (left) the Coleambally in NSW and (right) the DoE ARM SGP site. The range of water vapor amounts used is from 0.9–1.5 cm for the left panel and from 0.5–1.1 cm for the right panel, and therefore, the range of the scale on the left-hand side is 0.6 cm. The mean water vapor amount for Coleambally is 1.17 cm, and the mean amount for the SGP is 0.83 cm. The resolution of the water vapor calculation used to generate these images is 0.02 cm.

leaf water absorption variations that are present in both the 945- and 1125-nm water vapor absorption bands. Fig. 12 shows images of water vapor amounts for Coleambally and the ARM SGP site. Although there are extremely strong soil/vegetation contrasts in the Coleambally imagery, these are not particularly apparent in the water vapor image. In the SGP water vapor image, the highest water vapor amounts are over water and a very dark area of the land surface and are indicative of the method failing over these dark surfaces. Similarly to the Coleambally image, the contrasts in the water vapor retrievals over soil and vegetation at the SGP are not particularly strong ($<$0.1 cm). The water vapor amount at the SGP measured by a Multi-Filter Rotating Shadow-band Radiometer (MFRSR) [69], which is tuned to match the microwave radiometer (MWR) column water amounts, is 0.59 cm, while the retrieved mean water vapor amount for the SGP image is 0.82 cm with a standard deviation of 0.07 cm. This high bias is in contrast to recent comparisons between sun photometer water vapor retrievals using the 945-nm water vapor band and MWR retrievals of water vapor [68]. In that comparison, the sun photometer estimates were biased low compared with the microwave estimates. It should be noted, however, that this is only a single case and that the water vapor amount in this instance is less than any that was present in the intercomparison and is biased high by the inclusion of retrievals over the river and dark land surface. For Coleambally, the mean retrieved water vapor amount is 1.17 cm with a standard deviation of 0.08 cm. These estimated water vapor amounts using HITRAN 2000 are the same (SGP) or 0.1 cm less (Coleambally) than estimates using a corrected version of HITRAN 96. This is consistent with the relatively small overall band strength differences between HITRAN 96 and HITRAN 2000 in the 1125-nm water vapor band that is used here. The predominant artifact in the water vapor retrieval images is the striping that is caused by small calibration variations across the SWIR FPA. This problem can be mitigated in the processing by picking the window to which the water vapor band should be normalized to be consistent with the surrounding pixels. Here we have presented the results of the analysis as it is described above to indicate the relative magnitude of the contributions of surface and calibration to the biases and random errors in the retrieval of water vapor using the Hyperion SWIR FPA.

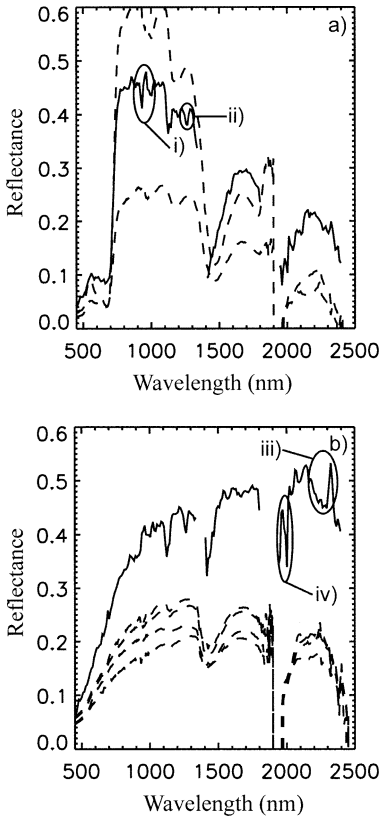

Fig. 13. Atmospherically corrected Hyperion data aquired on October 16, 2001 (solid lines) compared with *in situ* surface measurements made between August 14–19, 2001 (dashed lines). (a) Vegetation spectrum. (b) Soil spectrum.

C. Atmospherically Corrected Spectra

In Fig. 13, Hyperion data acquired on October 16, 2001 that has been atmospherically corrected is shown with some *in situ* spectra that were measured between August 14–19, 2001 in the same areas, presented as a point of reference. In the vegetation spectrum [Fig. 13(a)] two artifacts are noted. Artifact (i) is a result of the correction of the wings and center of the 945-nm band not being consistent: the correction of the band wings appears to be reasonable (consistent with liquid water in the corrected spectrum), but the band center is overcorrected. The aerosol load was low on this day (0.045 at 865 nm), and so the dominant correction term is the direct beam transmission. Therefore, it seems unlikely that this is the cause of this artifact, and the fact that this spectral domain is at the edge of the response of both the VNIR and SWIR detectors may be an issue. Artifact (ii) is in the spectral region where there is oxygen absorption. Given the extremely good correction of the oxygen A and B bands in the VNIR part of the spectrum and the fact that the depth of the water vapor absorption feature at 1125 nm is broadly consistent with observed water vapor amounts, the cause of this artifact is a mystery. In the soil spectrum [Fig. 13(b)] two further artifacts are noted. Artifact (iii) is large feature in the soil reflectance that has similar shape to methane absorption in this region. Tests with varying methane amounts and shifting the spectral locations of the Hyperion bands indicate that this feature is a real

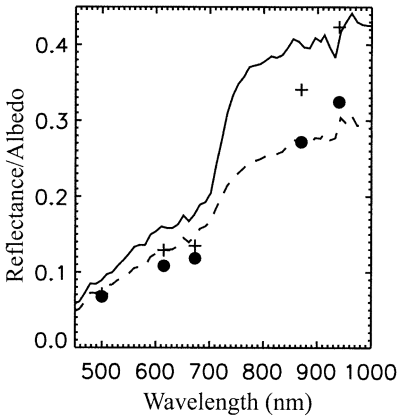

Fig. 14. Atmospherically corrected Hyperion data aquired on October 16, 2001 compared with downward-looking MFRSR albedo measurements made at the same time from 10-m (solid symbols) and 25-m (crosses) towers. The Hyperion data that best matches the location of the 10-m tower is shown as a dashed line, and the pixels that best match the location of the 25-m tower are shown as a solid line.

part of the data. Artifact (iv) is related to the problem noted earlier in the paper that it is not possible to match both centers and windows of the carbon dioxide band near 2000 nm, even though the overlap approximation used here agrees with line-by-line calculations and water vapor amounts are extremely low. The overall impression in comparing the atmospherically corrected Hyperion data with the *in situ* measurements made two months earlier is that it is much drier in October: the soil is brighter, and the number of pixels with vegetation spectra as clear as the one shown in Fig. 13(a) is limited; most show a mixture of soil and vegetation.

In Fig. 14, we compare atmospherically corrected Hyperion data with *in situ* data for the same time and location, October 16, 2001 at the ARM SGP Central Facility. There are two towers with a downward-looking MFRSR [69] mounted on them at 10 m on one tower and 25 m on the other tower. The MFRSR data are limited to spectral bands at 415, 500, 615, 673, 870, and 940 nm. The Hyperion data were segregated into pixels that best match the location of the 10-m tower and pixels that best match the location of the 25-m tower. Generally, the agreement is quite good for both sets of data (± 0.02 reflectance units) with the worst case being the 870-nm measurements for the 25-m tower where the Hyperion data are brighter by 0.04 reflectance units. Any more detailed explanation of these discrepancies would require bidirectional reflectance measurements, since the MFRSR measurements are an albedo measurement, while the Hyperion data are a nadir reflectance.

IV. Conclusion

The method described here to calculate the multiple-scattering properties required for atmospheric correction appears to have considerable promise in terms of allowing accurate calculations to be performed very rapidly, with the potential to perform near-real-time atmospheric correction. A particular advantage of this approach is that because the scattering calculations and the resolution of the line absorption calculations are decoupled, it is straightforward to perform calculations at any spectral resolution, provided k distributions are available at the required resolution, or line-by-line calculations from which such distributions can be calculated are available. The comparisons of the "random" overlap method with line-by-line calculation demonstrate that this approximation is adequate for 10-nm bandwidth instruments in the vicinity of 2000 nm where gaseous overlap is a particular problem.

The analysis of Hyperion data demonstrates the ability to use the speed and simplicity of the atmospheric correction code described herein to characterize the instrument and to retrieve water vapor amount with little surface contamination (<0.1 cm). The small variation in normalized spectral reflectance across a scan line for data taken at the SGP, where the surface is relatively uniform, demonstrates that the response of the SWIR FPA is relatively uniform across the spatial dimension of the FPA.

It is clear, given the significant "smile" on the VNIR FPA of Hyperion, that any atmospheric correction code that is used with Hyperion data should allow the band centers to vary as a function of spatial location and should allow the band centers of the SWIR and VNIR FPAs to be specified independently. These lessons are being incorporated into a public release of the atmospheric correction code that is described in this paper.

Acknowledgment

The authors would like to thank M. Miller (Department of Energy's ARM program), J. Michalsky (SUNY Albany), and A. Trishchenko (Canada Center for Remote Sensing) for providing validation data. The criticisms and suggestions of two anonymous reviewers are also gratefully acknowledged.

References

[1] R. E. Turner and M. M. Spencer, "Atmospheric model for correction of spacecraft data," in *Proc. 8th Int. Symp. Remote Sensing of the Environment*, Ann Arbor, MI, 1972, pp. 895–934.

[2] W. A. Pearce, "A study of the effects of the atmosphere on Thematic Mapper observations," NASA, Greenbelt, MC, Applied Syst. Dept. Rep. 004-77, NASA-CR-166 660, 1977.

[3] J. V. Dave, "Effect of atmospheric conditions on remote sensing of a surface nonhomogeneity," *Photogramm. Eng. Remote Sens.*, vol. 46, pp. 1173–1180, 1980.

[4] D. Tanré, M. Herman, and P.-Y. Deschamps, "Influence of the background contribution upon space measurements of ground reflectance," *Appl. Opt.*, vol. 20, pp. 3676–3684, 1981.

[5] R. S. Fraser and Y. J. Kaufman, "The relative importance of aerosol scattering and absorption in remote sensing," *IEEE Trans. Geosci. Remote Sensing*, vol. GE-23, pp. 625–633, 1985.

[6] Y. J. Kaufman and C. Sendra, "Algorithm for automatic atmospheric corrections to visible and near-IR satellite imagery," *Int. J. Remote Sens.*, vol. 9, pp. 1357–1381, 1988.

[7] D. Tanré, C. Deroo, and P. Dahaut, "Effets atmosphériques en télédétection-logiciel de simulation du signal satellitaire dans le spectre solaire," in *Proc. 3rd Int. Colloq. Spectral Signatures of Objects in Remote Sensing*. Paris, France: European Space Agency, 1985, pp. 315–319.

[8] ——, "Simulation of the satellite signal in the solar spectrum (5S)," in *User's Guide, Laboratoire d'Optique Atmospherique*, Villeneuve d'Ascq, France, 1986, U.S.T. de Lille, 59 655.

[9] D. Tanré, C. Deroo, P. Dahaut, M. Herman, J. J. Morcrette, J. Perbos, and P.-Y. Deschamps, "Description of a computer code to simulate the satellite signal in the solar spectrum: The 5S code," *Int. J. Remote Sens.*, vol. 11, pp. 659–668, 1990.

[10] B.-C. Gao, K. B. Heidebrecht, and A. F. H. Goetz, "Derivation of scaled surface reflectance from AVIRIS data," *Remote Sens. Environ.*, vol. 44, pp. 165–178, 1993.

[11] J. E. Conel, "Determination of surface reflectance and estimates of atmospheric optical depthand single-scattering albedo from Landsat Thematic Mapper data," *Int. J. Remote Sens.*, vol. 11, pp. 783–828, 1990.

[12] J. F. de Haan, J. W. Hovenier, J. M. M. Kokke, and H. T. C. van Stokkom, "Removal of atmospheric influences on satellite borne imagery: A radiative transfer approach," *Remote Sens. Environ.*, vol. 37, pp. 1–21, 1991.

[13] R. Richter, "A fast atmospheric correction algorithm applied to Landsat TM images," *Int. J. Remote Sens.*, vol. 11, pp. 159–166, 1990.

[14] ——, "A spatially adaptive fast atmospheric correction algorithm," *Int. J. Remote Sens.*, vol. 17, pp. 1201–1214, 1996.

[15] A. Berk, L. S. Bernstein, G. P. Anderson, P. K. Acharya, D. C. Robertson, J .H. Chetwynd, and S. M. Adler-Golden, "MODTRAN cloud and multiple scattering upgrades with application to AVIRIS," *Remote Sens. Environ.*, vol. 65, p. 367, 1998.

[16] M. W. Matthew *et al.*, "Status of atmospheric correction using a MODTRAN4-based algorithm," in *Summaries of the 9th Annu. JPL Earth Science Workshop*, vol. 1, 2000, http://makalu.jpl.nasa.gov.

[17] D. Schlapfer, C. C. Borel, J. Keller, and K. I. Itten, "Atmospheric precorrected differential absorption technique to retrieve columnar water vapor," *Remote Sens. Environ.*, vol. 65, pp. 353–366, 1998.

[18] Z. Qu, A. F. H. Goetz, and K. B. Heidebrecht, "High Accuracy Atmosphere Correction for Hyperspectral data (HATCH)," in *Summaries of the 9th Annu. JPL Earth Science Workshop*, vol. 1, 2000, http://makalu.jpl.nasa.gov.

[19] R. O. Green, "Atmospheric water vapor sensitivity and compensation requirement for Earth-looking imaging spectrometers in the solar-reflected spectrum," *J. Geophys. Res.*, vol. 106, pp. 17 443–17 452, 2001.

[20] B.-C. Gao and A. F. H. Goetz, "Column atmospheric water vapor and vegetation liquid water retrievals from airborne imaging spectrometer data," *J. Geophys. Res.*, vol. 95, pp. 3549–3564, 1990.

[21] Y. J. Kaufman, *et al.*, "The MODIS 2.1μm channel—Correlation with visible reflectance for use in remote sensing of aerosol," *IEEE Trans. Geosci. Remote Sensing*, vol. 35, pp. 1286–1298, Sept. 1997.

[22] Y. J. Kaufman, D. Tanre, L. A. Remer, E. F. Vermote, A. Chu, and B. N. Holben, "Operational remote sensing of tropospheric aerosol over land from EOS Moderate Imaging Spectroradiometer," *J. Geophys. Res.*, vol. 102, p. 17 051, 1997.

[23] J. E. Conel, R. O. Green, G. Vane, C. J. Bruegge, R. E. Alley, and B. Curtiss, "Airborne Imaging Spectrometer-2: Radiometric spectral characteristics and comparison of ways to compensate for the atmosphere," *Proc. SPIE*, vol. 834, pp. 140–157, 1987.

[24] R. O. Green, J. E. Conel, J. Margolis, C. Bruegge, and G. Hoover, "An inversion algorithm for retrieval of atmospheric and leaf water absorption from AVIRIS radiance with compensation for atmospheric scattering," in *Proc. 3rd AVIRIS Workshop*, R. O. Green, Ed. Pasadena, CA: JPL, 1991.

[25] V. Carrere and J. E. Conel, "Recovery of atmospheric water vapor total column abundance from imaging spectrometer data around 940 nm—Sensitivity analysis and applications to Airborne Visible/Infrared Imaging Spectrometer (AVIRIS) data," *Remote Sens. Environ.*, vol. 44, pp. 179–204, 1993.

[26] C. G. Gelpi, "Removing path-scattered radiance from over-ocean spectrometer images for water vapor estimation," *Remote Sens. Environ.*, vol. 74, pp. 414–421, 2000.

[27] A. Rodger and M. J. Lynch, "Determining atmospheric column water vapor in the 0.4–2.5 micron spectral region," in *Proc. 10th AVIRIS Workshop*, R. O. Green, Ed. Pasadena, CA: JPL, 2001, pp. 321–330.

[28] R. Frouin, P.-Y. Deschamps, and P. Lecomte, "Determination from space of atmospheric total water vapor amounts by differential absorption near 940 nm: Theory and airborne verification," *J. Appl. Meteorol.*, vol. 29, pp. 448–459, 1990.

[29] Y. J. Kaufman and B.-C. Gao, "Remote sensing of water vapor in the near IR from EOS/MODIS," *IEEE Trans. Geosci. Remote Sensing*, vol. 30, pp. 871–884, Sept. 1992.

[30] M. D. Alexandrov, A. A. Lacis, B. E. Carlson, and B. Cairns, "Derivation of 2D fields of aerosol and trace gases parameters by integrated analysis of multi-instrument MFRSR dataset from DOE ARM Program CART site," *Proc. SPIE*, vol. 4539, 2001.

[31] B. Cairns, M. I. Mishchenko, L. D. Travis, and J. Chowdhary, "Aerosol retrievals over land surfaces (The Advantages of Polarization)," in *Proc. AMS Annu. Meeting*, Albuquerque, NM, Jan. 2001.

[32] R. O. Green, "Spectral calibration requirement for earth-looking imaging spectrometers in the solar-reflected spectrum," *Appl. Opt.*, vol. 37, pp. 683–690, 1998.

[33] ——, "Determination of the in-flight spectral and radiometric characteristics of the Airborne Visible/Infrared Imaging Spectrometer (AVIRIS)," in *Imaging Spectrosocopy: Fundamentals and Prospective Applications*, F. Toselli and J. Bodechtel, Eds. London, U.K.: Kluwer, 1992, pp. 103–123.

[34] P. Strobl, A. Mueller, D. Schlaepfer, and M. Schaepman, "Laboratory calibration and in-flight validation of the Digital Airborn Imaging Spectrometer DAIS 7915," *Proc. SPIE*, vol. 3071, pp. 225–236, 1997.

[35] T. G. Chrien, R. O. Green, C. J. Chovit, M. L. Eastwood, and C. M. Sarture, "Calibration of the airborne visible/infrared imaging spectrometer in the laboratory," in *Summaries 6th Annual JPL Airborne Earth Science Workshop*. Pasadena, CA: JPL, Mar., 4–8 1996, pp. 39–48.

[36] J. Lean, "Evolution of the sun's spectral irradiance since the Maunder Minimum," *Geophys. Res. Lett.*, vol. 27, pp. 2425–2428, 2000.

[37] C. Frohlich and J. Lean, "The Sun's total irradiance: Cycles, trends and climate change uncertainties since 1976," *Geophys. Res. Lett.*, vol. 25, pp. 4377–4380, 1998.

[38] G. Thuillier, M. Hersé, P.C. Simon, D. Labs, H. Mandel, D. Gillotay, and T. Foujols, "The visible solar spectral irradiance from 350 to 850 nm as measured by the SOLSPEC spectrometer during the ATLAS I mission," *Solar Phys.*, vol. 177, pp. 41–61, 1998.

[39] R. L. Kurucz, "The solar spectrum," in *Solar Interior and Atmosphere*, A. N. Cox, W. C. Livingston, and M. S. Matthews, Eds. Tucson, AZ: Univ. Arizona Press, 1991, pp. 663–669.

[40] A. C. Van de Hulst, "A new look at multiple scattering," NASA Goddard Institute for Space Studies, New York, Tech. Rep., 1962.

[41] W. M. Irvine, "Multiple scattering in planetary atmospheres," *Icarus*, vol. 25, pp. 175–204, 1975.

[42] P. C. Waterman, "Matrix-exponential description of radiative transfer," *J. Opt. Soc. Amer.*, vol. 71, pp. 410–422, 1981.

[43] A. Benedetti, P. Gabriel, and G. L. Stephens, "Properties of reflected sunlight from a Green's function method," *J. Quant. Spectroscop. Radiat. Transfer*, vol. 72, pp. 201–225, 2002.

[44] J. E. Hansen and L. D. Travis, "Light scattering in planetary atmospheres," *Space Sci. Rev.*, vol. 16, pp. 527–610, 1974.

[45] J. F. de Haan, P. B. Bosma, and J. W. Hovenier, "The adding method for multiple scattering calculations of polarized light," *Astronom. Astrophys.*, vol. 183, pp. 371–391, 1987.

[46] S. Twomey, "Doubling and superposition methods in the presence of thermal emission," *J. Quant. Spectroscop. Radiat. Transfer*, vol. 22, pp. 355–363, 1974.

[47] S. Platnick, "A superposition technique for deriving mean photon scattering statistics in plane parallel cloudy atmospheres," *J. Quant. Spectroscop. Radiat. Transfer*, vol. 68, pp. 57–73, 2001.

[48] B. Cairns, B. E. Carlson, A. A. Lacis, and E. E. Russell, "An analysis of ground-based polarimetric sky radiance measurements," *Proc. SPIE*, vol. 3121, pp. 383–393, 1997.

[49] T. Nakajima, G. Tonna, R. Rao, P. Boi, Y. J. Kaufman, and B. N. Holben, "Use of sky brightness measurements from the ground for remote sensing of particulate polydispersions," *Appl. Opt.*, vol. 35, pp. 2672–2686, 1996.

[50] L. P. Giver, C. Chackerian, Jr., and P. Varanasi, "Visible and near-infrared H2O line intensity correction for Hitran-96," *J. Quant. Spectroscop. Radiat. Transfer*, vol. 66, pp. 101–105, 2000.

[51] R. M. Goody and Y. L. Yung, *Atmospheric Radiation: Theoretical Basis*. New York: Oxford Univ. Press, 1989, pp. 125–188.

[52] A. A. Lacis and V. Oinas, "A description of the correlated k distribution method for modeling nongray gaseous absorption, thermal emission and multiple scattering in vertically inhomogeneous atmospheres," *J. Geophys. Res.*, vol. 96, pp. 9027–9063, 1991.

[53] Q. Ma and R. H. Tipping, "A far line shape theory and its application to the water continuum absorption in the infrared region. I," *J. Chem. Phys.*, vol. 95, pp. 6290–6301, 1991.

[54] E. F. Vermote *et al.*, "Second simulation of the satellite signal in the solar spectrum (6S)," NASA Goddard Space Flight Center, Greenbelt, MD, 6S User Guide Ver. 6.0, 1994.

[55] R. Richter, "Atmospheric correction of DAIS hyperspectral image data," *Proc. SPIE*, vol. 2758, 1996.

[56] E. F. Vermote *et al.*, "Atmospheric correction of visible to middle infra-red EOS-MODIS data over land surfaces: Background, operational algorithm and validation," *J. Geophys. Res.*, vol. 102, pp. 17131–17 141, 1997.

[57] P. Mouroulis, R. O. Green, and T. G. Chrien, "Design of pushbroom imaging spectrometers for optimum recovery of spectroscopic and spatial information," *Appl. Opt.*, vol. 39, pp. 2210–2220, 2000.